PROCEEDINGS A

royalsocietypublishing.org/journal/rspa

Research

Cite this article: Himmelmann M, Pedersen MC, Klatt MA, Schönhöfer PWA, Evans ME, Schröder-Turk GE. 2026 Amorphous bicontinuous minimal surface models and the superior Gaussian curvature uniformity of diamond, primitive and gyroid surfaces. *Proc. R. Soc. A* **482**: 20250275. https://doi.org/10.1098/rspa.2025.0275

Received: 28 March 2025
Accepted: 17 November 2025

Subject Areas:
applied mathematics, materials science

Keywords:
triply periodic minimal surfaces, embedding theorem, Helfrich and Willmore functionals, Lonsdaleite, amorphous diamond

Author for correspondence:
M. Himmelmann
e-mail: matthias_himmelmann@brown.edu

Amorphous bicontinuous minimal surface models and the superior Gaussian curvature uniformity of diamond, primitive and gyroid surfaces

M. Himmelmann[1,2], M. C. Pedersen[3], M. A. Klatt[4,5,6], P. W. A. Schönhöfer[7], M. E. Evans[1] and G. E. Schröder-Turk[3,8,9,10]

[1]Institute for Mathematics, Universität Potsdam, Potsdam, Germany
[2]ICERM, Brown University, Providence, RI, USA
[3]Niels Bohr Institute, Københavns Universitet, Copenhagen, Denmark
[4]German Aerospace Center (DLR), Institute for AI Safety and Security, Ulm, Germany
[5]German Aerospace Center (DLR), Institute of Frontier Materials on Earth and in Space, Functional, Granular, and Composite Materials, Cologne, Germany
[6]Department of Physics, Ludwig-Maximilians-Universität München, Munich, Germany
[7]Department of Chemical Engineering, University of Michigan, Ann Arbor, MI, USA
[8]School of Mathematics, Statistics, Chemistry and Physics, Murdoch University, Perth, Australia
[9]Research School of Physical Sciences, The Australian National University, Acton, Australia
[10]Department of Chemistry, Technical University of Denmark, Kongens Lyngby, Denmark

MH, 0000-0002-5655-6740; MCP, 0000-0002-8982-7615; MAK, 0000-0002-1029-5960; PWAS, 0000-0003-4397-2937; MEE, 0000-0002-0161-6523; GEST, 0000-0001-5093-415X

Electronic supplementary material is available online at https://doi.org/10.6084/m9.figshare.c.8174484.

THE ROYAL SOCIETY
PUBLISHING

Bicontinuous geometries, both ordered and amorphous, are commonly found in many soft matter systems. Ordered bicontinuous phases can be modelled by periodic minimal surfaces, including Schoen's gyroid (G) or Schwarz' primitive (P) and diamond (D) surfaces. By contrast, a minimal surface model for amorphous phases has been lacking. Here, we study minimal surface models for amorphous bicontinuous phases, such as sponge phases. Using the surface evolver with a novel topology-stabilizing minimization scheme, we numerically construct amorphous minimal surfaces from both a continuous random network (CRN) model for amorphous diamond and from a randomly perforated parallel sheet model. As per Hilbert's embedding theorem, the Gaussian curvature of these surfaces cannot be constant. Our analysis of Gaussian curvature variances finds no substantial long-wavelength curvature variations in the amorphous diamond minimal surfaces. However, their Gaussian curvature variance is substantially larger than that of the cubic P, D and G surfaces. Our work demonstrates the superior curvature homogeneity of the cubic P, D and G surfaces compared to their entropy-favoured amorphous counterparts and to other periodic minimal surfaces. This general geometric result is relevant to bicontinuous structure formation in soft matter and biology across all length scales.

1. Introduction

Hilbert's famous embedding theorem [1] stipulates that in our Euclidean space $\mathbb{E}^3$, an infinite smooth saddle-shaped surface cannot have constant Gaussian curvature. Any physical system that strives for constant negative Gaussian curvature is necessarily frustrated. A 'perfect' interface with constant negative Gaussian curvature—as idealized by the hyperbolic plane $\mathbb{H}^2$—does not exist in $\mathbb{E}^3$. In the absence of a perfect interface, the fundamental question for any real-world system is: which saddle-shaped interface has the least variation in Gaussian curvature?

Figure 1 illustrates this question. Local constructions for surface patches in $\mathbb{E}^3$ with constant Gaussian curvature equal to -1 exist, as illustrated by crocheted hyperbolic corals [2,6] and other hyperbolic sculptures [7] or by the pseudosphere [8]. However, when sufficiently extended such surfaces lose their smoothness (C^2 differentiability), they may also develop self-intersections and they cannot be minimal.[1] By contrast, triply periodic minimal surfaces (TPMS), including Alan Schoen's gyroid surface, are infinite and smooth saddle surfaces. Consequently, their Gaussian curvature varies across the surface; their Gaussian curvatures density function is non-zero over a finite range of values (figure 1e).

In the context of soft matter and biological membranes, curvature homogeneity is foremost relevant for the self-assembled phases based on bicontinuous minimal surfaces, such as the gyroid phase in copolymers [9,10], the bicontinuous cubic phases [11] or the biological intracellular bicontinuous cubic membranes [12]. Their bilayer, membrane or matrix mid-surface is given by a TPMS. Interface curvatures are central to modelling these phases, including in Helfrich-type bending functionals [13], the competition of surface tension with chain stretching terms [14–16] and the relationship between the molecular shape and interface curvatures [11,17].

Curvature distributions and variances have been analysed for cubic minimal surfaces [13,18] and for surface families that contain the cubic primitive (P), diamond (D) and gyroid (G) surfaces [19,20], see also earlier scalar measures of homogeneity [17,21]. Those analyses have found that these three cubic surfaces have the smallest Gaussian curvature variances among all investigated periodic minimal surfaces.

This raises two questions: first, are these three cubic minimal surfaces truly the best interface geometries in terms of minimizing curvature variations or has the best interface geometry just not yet been found? Second, what aspects of their geometry enable these cubic minimal surfaces to achieve their Gaussian curvature homogeneity? Some insight into these questions is afforded

---

[1] The Codazzi equation implies that no surface in $\mathbb{E}^3$ can, even locally, have $K = \kappa_1\kappa_2 = -1$ and be minimal, $H = (\kappa_1 + \kappa_2)/2 = 0 \Leftrightarrow \kappa_1 = -\kappa_2$, with κ_1, κ_2 the two principal curvatures, see theorem 2.6 in [8].

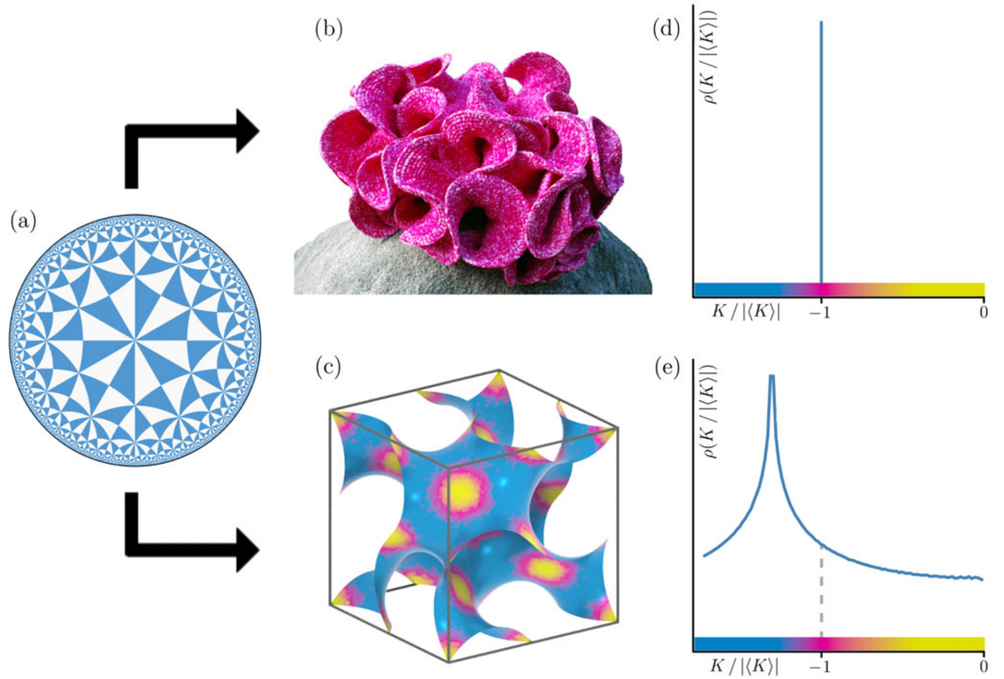

Figure 1. Gaussian curvatures and irregularity of saddle surfaces in $\mathbb{R}^3$. As per the embedding theorem, it is not possible to find a C^2 embedding of the hyperbolic plane $\mathbb{H}^2$ in $\mathbb{R}^3$ that maintains its constant Gaussian curvature $K = -1$. (a) Poincaré disc model of $\mathbb{H}^2$ decorated with the symmetric single-tile *246 tiling (colour is for presentation only). (b) The crocheted model for the hyperbolic plane by Taimina [2] has, by construction, constant Gaussian curvature with the curvature distribution, a δ function at $K = -1$. However, if extended infinitely, it would not be twice continuously differentiable and thus cannot have principal curvatures at all points [3] (image source: [2]). (c) Embedded TPMSs, here the gyroid, are smooth intersection-free saddle surfaces. The Gaussian curvature of such surfaces (represented by the surface colour) is negative, $\langle K\rangle = \chi/(2\pi A) < 0$ (where χ is the Euler–Poincaré index and A is the surface area). However, all TPMS have isolated flat points where the Gaussian curvature is equal to zero [4], and hence must have a Gaussian curvature distribution of finite width that includes a finite area patch near $K = 0$ [5, corollary 3.3]. (d) Gauss curvature distribution function for the hyperbolic plane; as $K = -1$, the distribution function is a δ-function at $K = -1$. (e) Gauss curvature distribution function for the gyroid (with $\langle K\rangle = -1$), showing finite values over a range of curvature values.

by comparing their curvature properties to those of amorphous bicontinuous minimal surfaces without periodicity.

Amorphous bicontinuous saddle surfaces are not only a reference point for their ordered counterparts, but are highly relevant in their own right. Any amorphous spatial network can be transformed into a ‘network solid’ (e.g. by tubifying [22]), bounded by an interface that is, on average, saddle-shaped with $\langle K\rangle = \chi/(2\pi A) < 0$. There is an abundance of systems that form amorphous and, on average, negatively curved interfaces, ranging from porous materials in geology, chemistry and biology, to phase separation processes such as spinodal decomposition, to biological membranes, sponge-like carbon phases and many others. While curvature homogeneity is probably relevant to many of these systems, it may be most pertinent to systems with interfaces close to minimal surfaces, such as in the L3 sponge phase in ternary lipid systems [23] or in the calcium carbonate skeleton of the sea urchin [24].

Synthetic amorphous meta-materials have garnered interest for optical applications [25,26] and biomaterial applications [27], largely owing to their isotropic material properties that cannot be achieved with crystalline structures. Given the interest in ordered bicontinuous geometries for tissue engineering and bone scaffold designs, it seems likely that amorphous bicontinuous minimal surfaces are valuable fully isotropic candidate structures for such applications.

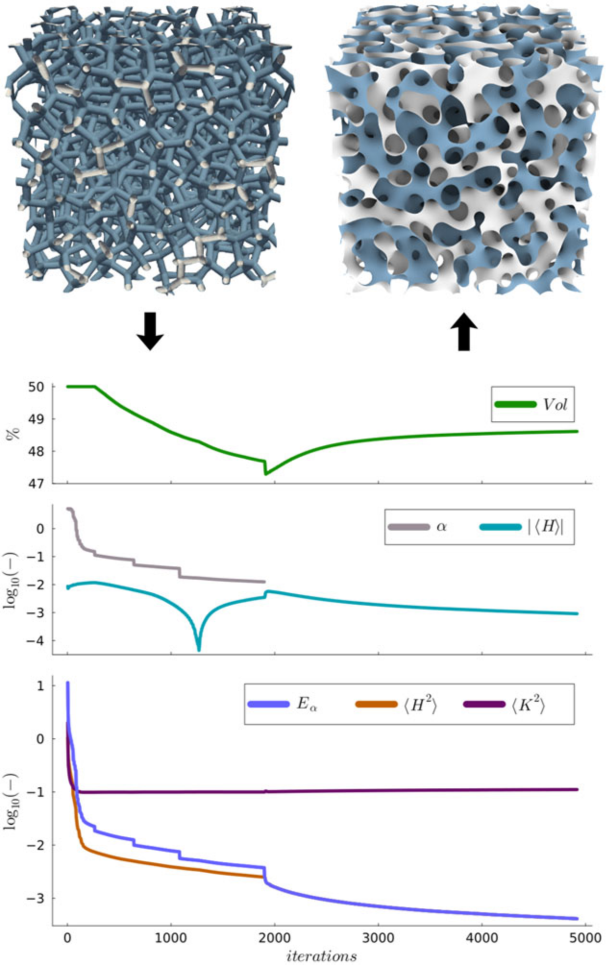

Figure 2. Evolution from a tubular initial configuration to a minimal surface under a topology-stabilized version of the Willmore functional. A surface mesh approximating an amorphous diamond minimal surface (bottom left) is obtained from an initial tubular representation of the amorphous diamond network (top left) by minimizing the functional $E_n(\mathcal{M})$, equation (4.1), using the Surface Evolver software [30]. In the initial stages, a term $\alpha(n)\int K^2\,dA$ penalizing high absolute values of Gaussian curvature is included with a modulus $\alpha(n)$ that decays as the evolution progresses; this term prevents 'pinch-off' effects, thereby stabilizing the topology and a smooth negatively curved surface.

Mathematically, the existence and curvature properties of amorphous bicontinuous minimal surfaces are open questions. We hope that the numerical construction algorithm presented here will inspire rigorous mathematical analyses of the existence and uniqueness of amorphous minimal surface forms, as well as their optimality with respect to higher-order integral Gaussian curvature properties. Such studies will probably involve random fields, specifically Gaussian random fields whose statistical Gaussian curvature properties have been studied in the context of microemulsion interfaces [28,29].

2. Results

(a) Minimal companion surfaces to the amorphous diamond net

Embedded minimal ($H=0$) companion surfaces of the amorphous diamond network can be generated by a robust minimization scheme in Surface Evolver [30], see §4a.

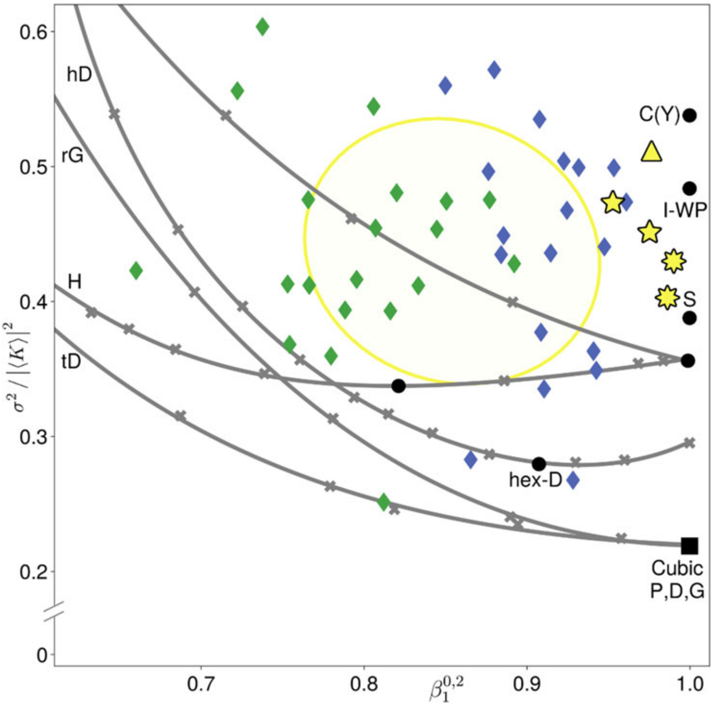

Figure 3. Gaussian curvature variance and isotropy of amorphous diamond minimal surface and of TPMS families. Gaussian curvature variances $\sigma^2/(\langle K\rangle)^2$ and isotropy indices $\beta_1^{0,2}$ are shown for realizations of differing size of the amorphous diamond minimal surface ($\chi = -432$ triangle, $\chi = -2000$ 5-star, $\chi = -8192$ 8-star), cubic subsets of all amorphous diamond samples at random positions and of various sizes (filled diamond symbols: $\chi = -16$ green, $\chi = -2^3 \times 16$ blue), TPMS with cubic symmetry (solid discs and square) and one-parameter TPMS families (solid lines). The ellipse represents a principal component analysis of data points from the cubic subsamples. For the construction of the hexagonal diamond minimal surface, refer to electronic supplementary material, §1.

Figure 2 shows the evolution of a tubular continuous random network (CRN) [31] under this topology-preserving algorithm. This demonstrates that embedded minimal ($H = 0$) companion surfaces of the amorphous diamond network exist, at least to a good numerical approximation. The second term in the objective function E_n in equation (4.1) prevents 'pinch-off' effects, such as the degeneration of catenoidal necks to a line (see electronic supplementary material, §4).

Converged solutions have average Willmore energy less than 10^{-3}, with pointwise mean curvatures very close to zero, $\langle H\rangle/|\langle K\rangle|^{1/2} < 10^{-6}$, with small standard and maximal deviations (see electronic supplementary material, table 2). We find no indication of emerging translational symmetry within the simulation box with periodic boundary conditions.

These surfaces, termed *amorphous diamond minimal surfaces*, are not balanced; the volumes of the two domains (labyrinths) differ, with the volume fraction of the domain that emerged from the original amorphous diamond network equal to 0.4837 ± 0.0064 (±variations across five realizations). See the channel thickness analysis in electronic supplementary material, §9 for further details.

(b) Variances of Gaussian curvature

The key result of this study is that the amorphous diamond minimal surfaces, while close to isotropic and more uniform in Gaussian curvature than other amorphous minimal surfaces, have significantly larger Gaussian curvature variances than the cubic P, D and G surfaces (figure 3). The Gaussian curvature variance is defined as $\sigma^2 = \langle (K^2 - \langle K\rangle)^2\rangle = \langle K^2\rangle - \langle K\rangle^2$. The average value $\langle K\rangle$ and the average square value $\langle K^2\rangle$ are calculated as $\langle K^n\rangle = (1/A)\int_S [K(p)]^n \,\mathrm{d}A$.

As the Gaussian curvature is a dimensional quantity, with SI unit $[K] = \mathrm{m}^{-2}$, the length scale needs to be set. Our analysis of $\sigma^2/(\langle K\rangle)^2$ corresponds to a length scale set such that the average Gaussian curvature is $\langle K\rangle = -1$.

The degree of anisotropy is measured using the isotropy index $\beta = \beta_1^{0,2} \in [0, 1]$ based on the second-rank (Minkowski) interface tensor [32,33]. A value of $\beta = 1$ indicates an interface that is isotropic in the sense that the eigenvalues of the rank-two interface tensor are all equal (this includes interfaces with cubic symmetry). Values below unity indicate anisotropic interfaces.

Figure 3 shows Gaussian curvature variances. The cubic P, D and G surfaces have the lowest, but finite, variance, with $\sigma^2/|\langle K\rangle|^2 \approx 0.2188$ (as the P, D and G surfaces are isometric when $\langle K\rangle = -1$, their variance value is the same). Here, division by $|\langle K\rangle|^2$ corresponds to length normalization such that $\langle K\rangle = -1$. Their isotropy is $\beta_1^{0,2} = 1$, reflective of their cubic symmetry.

The amorphous diamond surfaces have variances $\sigma^2/|\langle K\rangle|^2 > 0.4$, about twice as large as the cubic P, D and G surfaces. They are highly isotropic, with $\beta_1^{0,2} > 0.95$. $\sigma^2/|\langle K\rangle|^2$ decreases slightly with sample size.

A subset analysis of the $\chi = -5^3 \times 16$ amorphous diamond surfaces is performed with randomly placed cubic subsets whose size is chosen so that the average Euler characteristic is (-16) and $2^3 \times (-16)$, respectively. These random cubic subsets cut out surface patches from the amorphous diamond surfaces, which we refer to as *cubic subset samples*. The Gaussian curvature variances differ significantly between subsets (see principal component analysis in figure 3), but remain above the value of the cubic P, D, and G surfaces.

Figure 3 also shows data for one-parameter families of TPMS with non-cubic symmetry [20,34,35]. These families can be understood as deformations of particular members with higher symmetry (which for the tG, tD, tP, rG, rPD are the cubic P, D and G surfaces) or with particularly high spatial isotropy (the members of H and hexagonal diamond hD with $\beta_1^{0,2} = 1$). These deformations exhibit small continuous changes of $\sigma^2/|\langle K\rangle|^2$, at the expense of lesser isotropy. Like the H surface [35], the member of the hexagonal diamond family with the lowest curvature variance is not the most isotropic one.

(c) Distributions of Gaussian curvatures

Figure 4 shows distributions of Gaussian curvatures. The Gaussian curvature distribution function is $\rho(K) = \int_S \delta(K - K(p))\, \mathrm{d}A$ with the delta distribution δ and $\rho(K)\, \mathrm{d}K$ the total surface area of patches in S with Gaussian curvature between K and $K + \mathrm{d}K$.

For the cubic gyroid, the distribution is finite between 0 and $K/|\langle K\rangle| = -1.72$ where it sharply drops to 0. For all members of the rG family, the distributions extend from 0 to a value $K/|\langle K\rangle$, less than the value -1.72 of the cubic P, D and G surfaces, where the value sharply drops to zero (cf. electronic supplementary material, §14 for the behaviour of other surface families tD, tG, tP, rPD and H).

The Gaussian curvature distribution of the amorphous diamond surface, analysed over the $\chi = -5^3 \times 16$ sample, appears as a smooth function with a tail that continuously decays and reaches zero at $K/|\langle K\rangle| \approx -4$. It has a relatively broad and smooth maximum; the mode of the distribution (maximal value), at $K/|\langle K\rangle| \approx -0.45$, is greater than its average value (-1), different from the cubic P, D and G surfaces.

Guided by the first and third quartiles of the curvature distribution of the P, D and G surfaces, we set thresholds to define high, medium and low curvature as $K/|\langle K\rangle| < -1.36$, $K/|\langle K\rangle| \in [-1.36, -0.65)$ and $K/|\langle K\rangle| \in [-0.65, 0]$, respectively. Electronic supplementary material, table 3 provides the corresponding area fractions for all surfaces. The amorphous diamond surfaces have significantly larger area fractions of both low and high curvature than the P, D and G surfaces.

To discern inherent local curvature from larger-scale variations, the $\chi = -3^3 \times 16$ sample is subdivided into a grid of equal-sized cubic domains such that the average Euler–Poincaré number is $\chi = -8$ in each domain. Gaussian curvature distribution functions evaluated for individual domains fluctuate around the distribution for the whole surface and show no indication of sharp peaks.

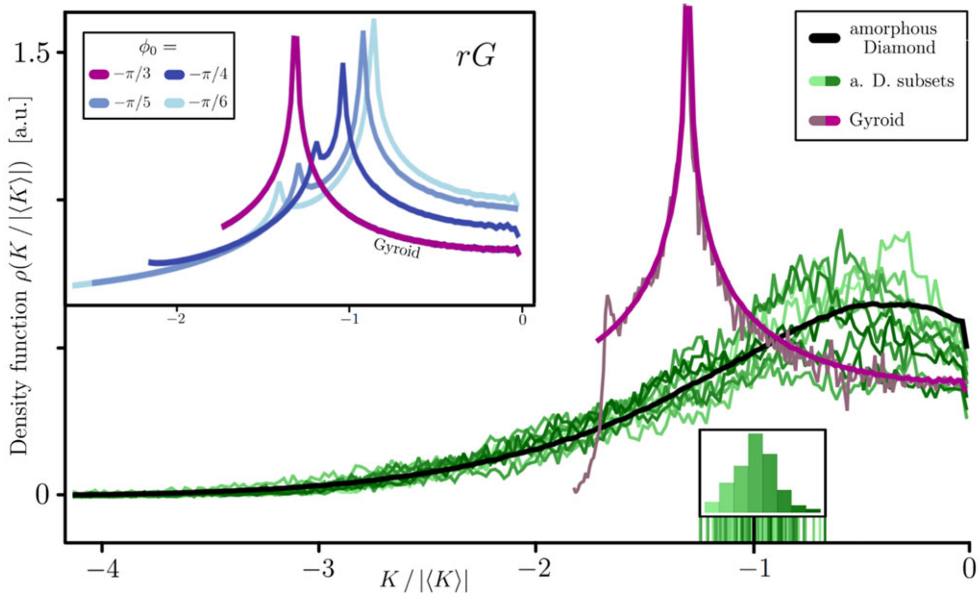

Figure 4. Curvature distributions of amorphous diamond surfaces and symmetry deformations of the cubic G surface. The main plot shows the curvature distribution function for the cubic gyroid (purple curve), for the $\chi = -8^3 \times 16$ sample of the amorphous diamond surface (black curve) and for ten randomly placed $\chi = -16$ cubic samples of that surface. The function $|\langle K\rangle|\rho(K/|\langle K\rangle|)$ is the density function when the length scale is normalized to give $\langle K\rangle = -1$. The insert shows distributions for various rG surface members, including the cubic gyroid as the member with $\phi_0 = \pi/3$. For each surface, there is a point of greatest curvature, where the minimal surface attains its most negative Gaussian curvature $K_{\min}$; this point is different for different surfaces. The distributions are finite between $K_{\min}$ and 0. (For the cubic gyroid, the flat point corresponds to symmetry point *6, the maximally curved point to symmetry *4 and the maximum at $K/|\langle K\rangle| = -1.30$ to symmetry *2.) The vertical green dashes above the x-axis near −1 are the averages of $\langle K\rangle_i$ in the cubic subset samples, and the bar chart their distribution.

A one-way analysis of variances confirms the absence of substantial large-scale curvature variations. The *within-sample* variance for the cubic subset sample i is $\sigma_w = \overline{\langle (K - \langle K\rangle_i)^2\rangle_i} = 0.3834$; here, $\langle x\rangle_i := (\int_{S_i} x\,\mathrm{d}A)/A_i$ is the average of x within the sample i, A_i is the surface area in the cubic subset samples i and $\overline{x} := \sum_{i=1}^{M}(A_i x)/A$ is the area-weighted average over all M cubic subset samples. With $\langle K\rangle$ (which is equal to $\overline{\langle K\rangle_i}$), the *between-samples* variance is $\sigma_b = \overline{\langle K\rangle_i - \langle K\rangle^2} = 0.012$. The value $F = \sigma_b/\sigma_w = 0.03 \ll 1$ demonstrates that the inherent Gaussian curvature variations within each samples are far greater than the larger-scale variations of average Gaussian curvatures between samples.

3. Interpretation and discussion

We have demonstrated the numerical construction of an amorphous analogue of the bicontinuous TPMS. Our algorithm for the amorphous diamond minimal surface enables its use in material design and as a model for amorphous phases.

In terms of its curvature properties, the amorphous minimal surfaces provide an (as of yet missing) reference point for the homogeneity of its periodic counterparts. None of the amorphous minimal surfaces come close in curvature homogeneity to the cubic P, D and G surfaces, which are again confirmed as the surfaces with the lowest degree of Gaussian curvature heterogeneity amongst all investigated surfaces. However, the amorphous diamond minimal surfaces are of similar Gaussian curvature homogeneity to other cubic TPMS, such as the S or I-WP surface.

(a) The amorphous diamond surface has significant Gaussian curvature variations, but no long-range variations

The Gaussian curvature heterogeneity of the amorphous D is a localized property. Its variations in Gaussian curvature are evident in small subsets of the surface, with only small variations between different subsets, see §2c. This finding is perhaps expected given the narrow distributions of bond angles and lengths [31]. This absence of long-range curvature variations, together with the high degree of isotropy, will probably enhance the surface's relevance as a model for self-assembled (equilibrium) sponge phases and its usefulness for metamaterial designs.

(b) The amorphous diamond surface is not balanced or self-dual, and exhibits channel thickness variations

In contrast to the cubic P, D and G surfaces, the amorphous diamond surface is *not* balanced. The two channels differ slightly in volume and in their channel thickness structure (see electronic supplementary material, fig. 9 and table 2). This lack of duality is not unexpected given that the amorphous diamond net combines elements of the self-dual cubic diamond net (adjacent four-coordinated nodes are rotated by 60°) and of the hexagonal diamond (Lonsdaleite; where adjacent four-coordinated nodes are aligned). The relation between these two nets and their corresponding surfaces is highlighted in figure 5. The Lonsdaleite net is not self-dual in the notion of [37] and its dual is the graphite net (see electronic supplementary material, §3). Moreover, the hexagonal diamond minimal surface is not balanced ($\phi \neq 1/2$, see electronic supplementary material, table 2). Although the primal amorphous diamond net is four-coordinated, our construction algorithm does not take into account the dual net at all (see electronic supplementary material, §2). As a consequence, the dual network is generally not four-coordinated, leading to imbalances and inhomogeneities in the resulting amorphous diamond minimal surface. In particular, this fact highlights that the self-duality of the skeletal graphs of the primitive, diamond and gyroid surfaces is a rare and special property among nets.

It remains an open question whether there is a self-dual amorphous minimal surface. Similarly, it is unclear if there is a relationship between self-duality (or lack thereof) and homogeneity, especially concerning variations in domain size rather than curvature homogeneity.

Further exploration of the amorphous version of the Laves graph (or *srs* net, which is the skeletal graph of the gyroid), proposed by Sellers *et al.* [38], would be highly relevant. In the cubic TPMS, differences in homogeneity related to domain sizes—and the resulting packing frustration—are key distinguishing features of the diamond and the gyroid surfaces [20,39,40]. Therefore, considering a gyroid-like rather a diamond-like amorphous net would be highly relevant.

In combination, the above discussion hints at the big overarching question of whether and how surface curvature homogeneity relates to the properties of the two skeletal graphs that the surface defines, such as links, angles, loops and other topological or combinatorial properties. Relationships of the skeletal graphs with the surface's Euler characteristic (related to the number, or density, of flat points) and symmetry (relating to the size of the asymmetric unit, see §3d) appear likely. Still, the correlation with more complex measures is harder to explore but of great interest; this particularly includes constructions generating the interfaces from 'mesatomic' volumetric units [41].

(c) Origin of the superior homogeneity of the cubic P, D and G surfaces

None of the amorphous minimal surfaces considered here come close in Gaussian curvature homogeneity to that of the cubic P, D and G surfaces. Among surfaces with a high degree of isotropy, these three cubic surfaces stand out; only their continuous symmetry deformations (including tD, tP, tG, rG and rPD) approach the same Gaussian curvature homogeneity; however, at the expense of a significantly lower isotropy.

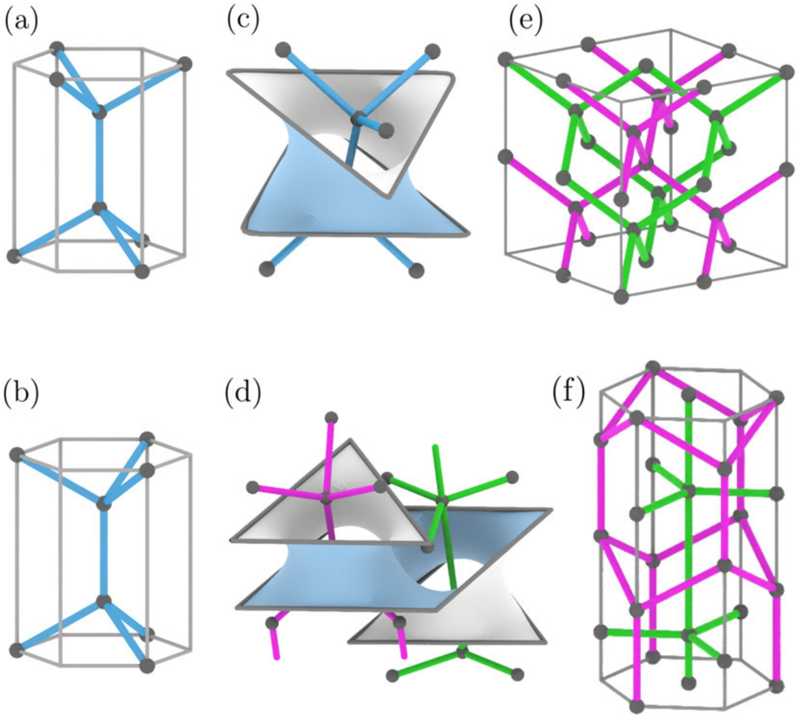

Figure 5. The three-periodic cubic diamond structure and the Lonsdaleite ('hexagonal diamond') structure and their dual nets. The diamond net *dia* (a) and the Lonsdaleite net *lon* (b), also known as hexagonal diamond, are generated from the same tetrahedral building block. Associated minimal surfaces are generated from triangular catenoidal frames, aligned with or without a 60° rotation (c,d). The translational unit cells of the diamond net (e) and Lonsdaleite structure (f) demonstrate the cubic and hexagonal symmetry, respectively, and also show the dual nets. The *dia* net is self-dual, leading to the well-known 'balanced' diamond structure where the diamond minimal surface separates two identical nets. The dual net of Lonsdaleite is the graphite net (*gra*, with three- and five-coordinated vertices); therefore the hexagonal diamond surface is not balanced and rather separates space into two domains of different shapes and volumes. For additional details on these nets, see [36].

How the P, D and G surfaces achieve their high degree of curvature homogeneity is elucidated by the curvature distributions: first, for any minimal surface, the curvature distribution extends from 0 (the flat points) to a maximum curvature value $-K_{\max}$. The P, D and G surfaces achieve a lower value of $K_{\max} > 0$ than all other surfaces studied here. Second, compared to other surfaces, the P, D and G surfaces keep the area fraction that corresponds to highly curved regions and to nearly flat regions, respectively, small; a bigger fraction of the surface has curvatures near the average Gaussian curvature of -1 (cf. electronic supplementary material, table 3).

(d) Cubic P, D and G surfaces confine curvature variations to the smallest possible asymmetric unit patch

The following two sections explore geometric aspects influencing a surface's curvature distribution, offering insights into why the cubic P, D and G surfaces hold a special status as the TPMS with the most uniform Gaussian curvature distribution.

If an embedded surface with constant Gaussian curvature $K = -1$ existed, its Gaussian curvature variance would, trivially, vanish. For *any* portion S of such a $K = -1$ surface, the surface area and Euler characteristic would be proportional,

$$A = -2\pi\chi, \tag{3.1}$$

by virtue of the Gauss–Bonnet theorem: $2\pi\chi = \int_S K\,\mathrm{d}A$ and as $\int_S K\,\mathrm{d}A = \int_S(-1)\,\mathrm{d}A = -\int_S \mathrm{d}A = -A$.

For a TPMS, this equation does not apply for arbitrary patches, as $K = -1$ cannot hold everywhere. However, *for any portion of a TPMS that is composed of an integer multiple of the asymmetric unit patch*,[2] equation (3.1) holds as $2\pi\chi = \int_S K\,\mathrm{d}A = A\langle K\rangle$ when the length scale is set so that $\langle K\rangle = -1$.

This means that TPMS confine Gaussian curvature fluctuations to a small patch—the asymmetric unit patch. There are no larger-scale curvature fluctuations (as the application of symmetries and translations do not change curvatures).

Importantly, the asymmetric unit patch of the cubic P and D surfaces—corresponding to the single-tile in the *246 tiling [42–44]—is the smallest possible unit patch from which a TPMS can be built, with 96 asymmetric unit patches each with $\chi(S_{\mathrm{asy}}) = -4/96 = -1/24$ required to construct the genus 3 translational unit cell. For the G surface, the asymmetric unit patch corresponds to the tile of the 246 tiling which is the union of two adjacent tiles of the *246 tiling. However, the intrinsic properties (Gaussian curvature) are the same for each half of the 246 tile.

This does not guarantee that the variance of Gaussian curvature is smallest for the P, D and G amongst all TPMS, as the argument says nothing about variations within the patch. However, it ensures that the variations are confined, by symmetry, to the smallest possible patch amongst all TPMS.

(e) Minimization of curvature variances by uniform placement of flatpoints akin to the quantizer problem

A TPMS is determined by the position and order of its flat points. This motivates a perspective where the flat points are viewed as the generators (and minima) of a monotonously increasing curvature function. Using a watershed concept, the surface can then be partitioned into Voronoi-like regions with respect to the curvature function. This perspective enables a comparison to the quantizer problem [45], and insights into the arrangement of flat points with the lowest curvature variance.

We adopt the perspective that the negative Gaussian curvature $-K$ is a scalar field on the surface where the flat points with $K = 0$ are local minima. In practice, it seems that there are no minima other than the N_f flat points at $\mathbf{r}_i$ $(i = 1, \ldots, N_f)$.

Using the concept of a watershed transform, the minimal surface (or its preimage in the complex or hyperbolic plane, or its multi-fold Gauss map) can be partitioned into patches C_i, which we refer to as '*regions*', each surrounding a flat point. That is, the (Riemannian) gradient descent path of $-K$ from each point in C_i ends at the flat point $\mathbf{r}_i$. This alludes to a possible construction of these regions via a gradient descent method restricted to the minimal surface, which is initialized with each vertex of its triangulation. With this approach, the surface is tessellated into exactly N_f regions, akin to a Voronoi partition in Euclidean space.

Up to a constant, the Gaussian curvature variance is a surface integral over the squared Gaussian curvature (with the usual $\langle K\rangle = -1$ normalization):

$$\sigma^2 = \langle K^2\rangle - (\langle K\rangle)^2 = \langle K^2\rangle - 1 = (1/A)\int_S K^2\,\mathrm{d}A - 1.$$

This integral can be broken up into a sum over contributions from each region, $\int_S K^2\,\mathrm{d}A = \sum_i \int_{C_i}[K(\mathbf{r})]^2\,\mathrm{d}A$.

If—as is not the case—$(-K(\mathbf{r}))$ was proportional to the distance to the nearest flat point ($K(\mathbf{r}) \propto d(\mathbf{r})$ where d is the distance field to the flat points) then the problem would correspond to a quantizer problem. The quantizer problem is defined for a set of points $\mathbf{r}_i$ in a space subject to an energy $E[\{\mathbf{r}_i\}] = \sum_i \int_{V_i}[d(\mathbf{r})]^2\,\mathrm{d}A$ where V_i is the Voronoi cell of point $\mathbf{r}_i$ and d is the Euclidean

---

[2] An asymmetric unit patch is the smallest patch of a TPMS from which the infinite surface can be generated by application of symmetries and translations.

distance map. The quantizer energy is minimized when the points are arranged such that their Voronoi cells have the same volume, are centred on their generating point and are as close to circular as the requirement to tessellate space allows. These uniform partitions are favoured because of the square in the integrand (or, more generally, the convexity of the integrand in d).

Our analysis in electronic supplementary material, fig. 11 shows that K is neither simply proportional to d, nor is it even a function of d alone. For the tG, tD, tP, rPD surface families, we find that, along paths emanating from the flat points in various radial directions, the Gaussian curvature is for small values of the in-surface distance d, a parabola: $K = -a \cdot d^2 + \text{h.o.t.}$ (the linear term vanishes), but the value a is not universal for all surfaces (electronic supplementary material, fig. 12). Also, for larger d, the curves differ from a parabola and vary for different directions (electronic supplementary material, fig. 11). Not unexpectedly, for the cubic P, D and G surfaces, the functions $K(d)$ show the greatest degree of homogeneity for different directions.

While there is no strict equivalence, the perspective of the quantizer problem remains useful and relevant. Controlling the variance of Gaussian curvature corresponds to controlling how far the Gaussian curvature can grow within a Voronoi-like region from its minimum at the flat point. Keeping variances low corresponds to avoiding large values of K. It appears that, just like in the quantizer problem, this is achieved by having many and therefore small regions (that means, having first-order flat points, rather than higher-order flat points), having regions centred on their generating flat point, uniformly sized regions and regions that are close to geodesic circles (which probably relates to the packing efficiency of the corresponding disc packing in $\mathbb{H}^2$ [46]).

The quantizer problem hence provides an interesting perspective on the question of optimal curvature homogeneity and motivates a future investigation of the relationships between hyperbolic tilings, disc packings and curvature variances.

4. Material and methods

(a) Topology-stabilized minimization scheme for minimal surface generation using the 'Surface Evolver'

Our curvature analysis is based on mesh models of minimal surfaces obtained using the 'Surface Evolver' programme [30], through an adaption of a Willmore flow process. Mesh surfaces are generated for which the Willmore functional (the integral of the squared mean curvature over the surface) equals zero within a small numerical tolerance, $\int [H(p)]^2 \,\mathrm{d}A = 0$, representing minimal surfaces with vanishing mean curvature $H(p) = 0$ for all points. These are obtained by iteratively adapting an initial coarse non-minimal polyhedral surface M, through an iterative scheme involving mesh refinement and minimization of the functional

$$E_n(\mathcal{M}) = \int_{\mathcal{M}} [H(p)]^2 \,\mathrm{d}A + \alpha(n) \cdot \int_{\mathcal{M}} [K(p)]^2 \,\mathrm{d}A, \tag{4.1}$$

where H and K are the mean and Gaussian curvature at a surface point p, the first term represents the Willmore energy $W[\mathcal{M}] = \int_{\mathcal{M}} [H(p)]^2 \,\mathrm{d}A$ and $\alpha(n)$ is a parameter that, from an initial positive value, decreases and is equal (or very close) to zero during the final stages of the minimization, see figure 2. For the first few iterations, a volume constraint, implemented through Lagrange multipliers, is enforced within the first iteration so that both domains (on either side of the surface) occupy exactly 50% of the volume.

The second term in electronic supplementary material, equation (4.1) stabilizes the initial stages of the iteration against pinch-off effects that change the topology of the surface by collapsing surface annuli to line-like objects without any area (see figure 6). For the evolution of high-genus structures without symmetry and pronounced variations in channel diameters, such pinch-off effects are common when minimizing the Willmore functional alone. In particular, these effects occur during our experiments (see electronic supplementary material, §4 for more details). By adding the Gaussian curvature term to $E_n[\mathcal{M}]$, we manage to stabilize the tendencies of narrow

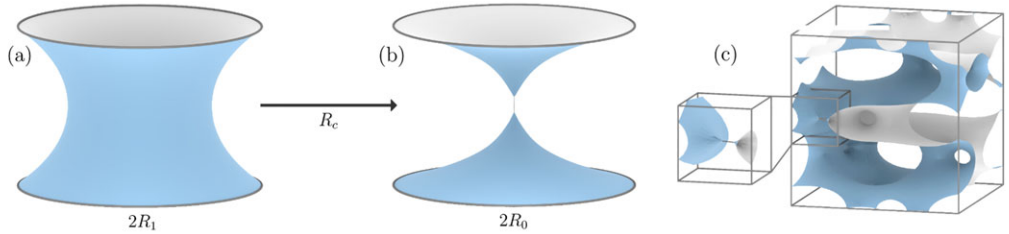

Figure 6. The pinch-off effect in the catenoid. From the soap film model's application to two parallel circular frames, the catenoid minimal surface can be constructed (a). It comes with a one-dimensional deformation family that is parametrized by the circle's radius, when fixing the catenoid's height to 2. There exists a critical radius $R_c \approx 1.50888$, where the catenoid collapses and 'pinches off' [47] (b). For radii $R_0 < R_c$, the only minimal surface inscribed in the two circles is the Goldschmidt solution consisting of two parallel discs. This behaviour can also be observed in the initial configurations produced by the algorithms from electronic supplementary material, §§3 and 7 that we use in our experiments (c).

catenoidal necks to collapse in the early stages of the optimization routine. An explanation for this phenomenon is that the Gaussian curvature term favours large flat regions and thus causes narrow catenoids to bulge outwards. This ultimately enables the algorithmic generation of the high-genus sections of the amorphous minimal surface models studied here.

(b) Generation of amorphous diamond minimal surfaces

Minimal surface mesh approximations (with $E \leq 10^{-3}$) were generated from tubular versions of the CRNs generated by Barkema & Mousseau [31]. Five separate realizations were investigated, within simulation boxes with periodic boundary conditions.

The resulting network structures are composed exclusively of tetravalent (four-coordinated) vertices. These network structures were inflated to a water-tight mesh representing a tubular version. The minimal surfaces obtained from these networks are referred to as 'amorphous diamond minimal surfaces'.

The size of a network or surface sample is conveniently characterized by its Euler characteristic χ which, like the surface area or toroidal volume, is additive and easy to calculate, and has the benefit of being dimensionless. For a four-valent network with N nodes, $\chi = -2N$ (see electronic supplementary material, §7). With $\chi = -16$, the Euler characteristic of the diamond surface's $Fd\bar{3}m$ unit cell (four nodes), $\chi/16$ conveniently measures the size in equivalent multiples of this diamond building block. (N is also the number of 'pants' in Thurston's pants decomposition [48].) Details of the amorphous diamond samples are listed in electronic supplementary material, table 2 and their sizes are $\chi = 3^3 \times (-16) = -432$, $\chi = 5^3 \times (-16) = -2000$ and $\chi = 8^3 \times (-16) = -8192$.

(c) Minimal surfaces from parallel layers with catenoidal connections

Further minimal surface approximations (with $E \leq 10^{-3}$) are obtained from an initial non-minimal mesh inspired by Chen [49], in which catenoidal necks are placed to connect adjacent layers in a stack of parallel planes under a repulsive lateral potential (see electronic supplementary material, §7 for details). A polyhedral mesh is constructed by an adaption of the set Voronoi diagram algorithm [50] implemented in `pomelo` [51]. The surface optimization scheme of §4a evolves these polyhedral meshes to minimal surfaces. Minimal surfaces with Euler characteristic up to $\chi = -180$ are examined with this model. Surfaces without or with low symmetry are favoured by choosing numbers of necks that are incompatible with regular arrangements.

(d) Curvature calculations and isotropy characterization for surface meshes

For the amorphous diamond surfaces and for the hexagonal diamond, C(Y), I-WP and S surfaces, Gauss and mean curvatures were calculated on triangulated mesh representations.

Details are listed in electronic supplementary material, table 2, with the finest meshes consisting of up to 12 300 triangles per χ. Pointwise and integral curvatures were determined using standard curvature routines implemented in Surface Evolver. For the tD, tG, tP, rPD, rG and H surfaces, Weierstrass parametrizations were used for the curvature calculations (see electronic supplementary material, §12).

A first-order measure of the orientational distribution of a surface $\mathcal{M}$ is given by the Minkowski tensor $W_1^{0,2} = \frac{1}{3}\int_{\mathcal{M}} \mathbf{n} \otimes \mathbf{n}\, \mathrm{d}A$ where $\mathbf{n}$ is the surface normal vector and the integration extends over the surface $\mathcal{M}$, as per [33]. The ratio $\beta_1^{0,2} \in [0,1] \subset \mathbb{R}$ of the smallest to the largest eigenvalue provides an indication of the degree of anisotropy. Surfaces with cubic symmetry and isotropic surfaces have $\beta = 1$; values $\beta < 1$ indicate an anisotropy in the orientational distribution of surface normal directions. Minkowski tensors were calculated with the programme `karambola` [32].

5. Concluding remarks

Research into bicontinuous minimal surfaces has seen a diverse range of approaches, including architectural soap film models, physical free energy modelling, structure enumeration, experimental and numerical mathematics and rigorous mathematical proofs (e.g. of embeddedness or uniqueness). The results of this article open up the rich ensemble of amorphous surfaces, with likely relevance to all of these research directions.

The specific question of which minimal surfaces minimize the curvature fluctuation $\sigma^2/\langle K\rangle^2$ may lend itself to a more rigorous mathematical analysis, perhaps informed by our results. For now, the hypothesis is that the cubic gyroid, diamond and primitive minimal surfaces represent the best solution stands. These surfaces may well be nature's best, albeit imperfect, attempt at embedding the hyperbolic plane in Euclidean space.

Data accessibility. Data are available at Zenodo: [52].

The data are provided in the electronic supplementary material [53].

Declaration of AI use. We have not used AI-assisted technologies in creating this article.

Authors' contributions. M.H.: conceptualization, data curation, formal analysis, investigation, methodology, software, validation, visualization, writing—original draft, writing—review and editing; M.C.P.: data curation, formal analysis, investigation, software, validation, visualization, writing—review and editing; M.A.K.: data curation, formal analysis, investigation, software, visualization, writing—review and editing; P.W.A.S.: formal analysis, methodology, software, writing—review and editing; M.E.E.: conceptualization, funding acquisition, methodology, supervision, writing—review and editing; G.E.S.-T.: conceptualization, formal analysis, methodology, supervision, validation, writing—original draft, writing—review and editing.

All authors gave final approval for publication and agreed to be held accountable for the work performed therein.

Conflict of interest declaration. We declare we have no competing interests.

Funding. G.E.S.-T. is grateful to Copenhagen University and the Danish Technical University for their hospitality and financial support, and to the Danish National Bank for accommodation in the picturesque Nyhavn 18 apartment. M.H. and M.E.E. are grateful for the financial support from the project 'Discretization in Geometry and Dynamics' (SFB 109) in the Deutsche Forschungsgemeinschaft (DFG). M.A.K. acknowledges funding and support by the Deutsche Forschungsgemeinschaft (DFG, German Research Foundation) through the SPP 2265, under grant nos. KL 3391/2-2, WI 5527/1-1 and LO 418/25-1, as well as by the Initiative and Networking Fund of the Helmholtz Association through the Project 'DataMat'. M.H. acknowledges the support by the National Science Foundation under grant no. DMS-1929284 while the author was in residence at the Institute for Computational and Experimental Research in Mathematics in Providence, RI, during the Geometry of Materials, Packings and Rigid Frameworks semester programme.

Acknowledgements. We are grateful to S.T. Hyde for valuable comments and for decades of scientific friendship and discussions that have shaped our thinking about minimal surface curvature homogeneity. We thank G.T. Barkema and N. Mousseau for providing their samples of CRNs and K. Polthier and M. Traizet for help and advice, and A. Hwang for the explanation using the Codazzi equation why constant Gaussian curvature surface patches cannot be minimal. We are grateful to S. Weis and K. Brakke whose freely available `pomelo`

Voronoi code and Surface Evolver code were used in this study. We thank A.M. Kraynik for help with the isotropy algorithm. We thank D. Taimina for permission to reproduce the image of the crocheted model in figure 1b.

References

1. Hilbert D. 1901 Über Flächen von constanter Gaussscher Krümmung. *Trans. Am. Math. Soc.* **2**, 87–99. (doi:10.2307/1986308)
2. Taimina D. 2009 Blog of Daina Taimina (accessed 2025-02-07).
3. Henderson DW. 2004 Extended hyperbolic surfaces in $\mathbb{R}^3$. *Proc. Math. Inst. Russ. Acad. Sci.* **247**, 267–279.
4. Hyde ST. 1989 The topology and geometry of infinite periodic surfaces. *Z. Kristallogr.* **187**, 165–185. (doi:10.1524/zkri.1989.187.3-4.165)
5. Meeks III WH. 1990 The theory of triply periodic minimal surfaces. *Ind. Univ. Math. J.* **39**, 877–936. (doi:10.1512/iumj.1990.39.39043)
6. Henderson D, Taimina D. 2001 Crocheting the hyperbolic plane. *Math. Intell.* **23**, 17–28. (doi:10.1007/BF03026623)
7. Goodman-Strauss C. 2017 What is up with Hilbert's embedding theorem. See https://chaimgoodmanstrauss.com/w-i-u-t-h-e-t/ (accessed 2025-02-07).
8. O'Neill B. 2006 *Elementary differential geometry*, 2nd edn. London, UK: Academic Press.
9. Park SJ, Bates FS, Dorfman KD. 2023 Single gyroid in H-shaped block copolymers. *Phys. Rev. Mater.* **7**, 105601. (doi:10.1103/PhysRevMaterials.7.105601)
10. Reddy A, Dimitriyev MS, Grason GM. 2022 Medial packing and elastic asymmetry stabilize the double-gyroid in block copolymers. *Nat. Commun.* **13**, 2629. (doi:10.1038/s41467-022-30343-2)
11. Hyde S, Blum Z, Landh T, Lidin S, Ninham B, Andersson S, Larsson K. 1996 *The language of shape: the role of curvature in condensed matter: physics, chemistry and biology*. Amsterdam, The Netherlands: Elsevier Science.
12. Almsherqi ZA, Landh T, Kohlwein SD, Deng Y. 2009 Chapter 6: cubic membranes the missing dimension of cell membrane organization. *Int. Rev. Cell Mol. Biol.* **274**, 275–342. (doi:10.1016/S1937-6448(08)02006-6)
13. Schwarz US, Gompper G. 2001 Bending frustration of lipidwater mesophases based on cubic minimal surfaces. *Langmuir* **17**, 2084–2096. (doi:10.1021/la0013805)
14. Anderson DM, Gruner SM, Leibler S. 1988 Geometrical aspects of the frustration in the cubic phases of lyotropic liquid crystals. *Proc. Natl Acad. Sci. USA* **85**, 5364–5368. (doi:10.1073/pnas.85.15.5364)
15. Schick M. 1998 Avatars of the gyroid. *Physica A* **251**, 1–11. (doi:10.1016/S0378-4371(97)00590-6)
16. Matsen MW, Bates FS. 1997 Block copolymer microstructures in the intermediate-segregation regime. *J. Chem. Phys.* **106**, 2436–2448. (doi:10.1063/1.473153)
17. Hyde ST. 1990 Curvature and the global structure of interfaces in surfactant-water systems. *J. Phys. Colloq.* **51**, C7-209–C7-228. (doi:10.1051/jphyscol:1990721)
18. Blanquer SBG *et al.* 2017 Surface curvature in triply-periodic minimal surface architectures as a distinct design parameter in preparing advanced tissue engineering scaffolds. *Biofabrication* **9**, 025001. (doi:10.1088/1758-5090/aa6553)
19. Fogden A, Hyde ST. 1999 Continuous transformations of cubic minimal surfaces. *Eur. J. Phys. B* **7**, 91–104. (doi:10.1007/s100510050592)
20. Schroeder-Turk GE, Fogden A, Hyde ST. 2006 Bicontinuous geometries and molecular self-assembly: comparison of local curvature and global packing variations in genus-three cubic, tetragonal and rhombohedral surfaces. *Eur. J. Phys. B* **54**, 509–524. (doi:10.1140/epjb/e2007-00025-7)
21. Hyde S, Ramsden S, Di Matteo T, Longdell J. 2003 Ab-initio construction of some crystalline 3D Euclidean networks. *Solid State Sci.* **5**, 35–45 (Dedicated to Sten Andersson for his scientific contribution to Solid State and Structural Chemistry). (doi:10.1016/S1293-2558(02)00079-1)
22. Bennett J, Vivodtzev F, Pascucci V. 2015 *Topological and statistical methods for complex data*, 1st edn. Mathematics and Visualization. Springer-Verlag, Berlin.
23. McGrath KM, Dabbs DM, Yao N, Edler KJ, Aksay IA, Gruner SM. 2000 Silica gels with tunable nanopores through templating of the L3 phase. *Langmuir* **16**, 398–406. (doi:10.1021/la990098z)

24. Jessop AL, Millsteed AJ, Kirkensgaard JJK, Shaw J, Clode PL, Schröder-Turk GE. 2024 Composite material in the sea urchin Cidaris rugosa: ordered and disordered micrometre-scale bicontinuous geometries. *J. R. Soc. Interface* **21**, 20230597. (doi:10.1098/rsif.2023.0597)
25. Klatt MA, Steinhardt PJ, Torquato S. 2021 Gap sensitivity reveals universal behaviors in optimized photonic crystal and disordered networks. *Phys. Rev. Lett.* **127**, 037401. (doi:10.1103/PhysRevLett.127.037401)
26. Yu S, Qiu CW, Chong Y, Torquato S, Park N. 2021 Engineered disorder in photonics. *Nat. Rev. Mater.* **6**, 226–243. (doi:10.1038/s41578-020-00263-y)
27. Kumar S, Tan S, Zheng L, Kochmann DM. 2020 Inverse-designed spinodoid metamaterials. *npj Comput. Mater.* **6**, 1–10. (doi:10.1038/s41524-020-0341-6)
28. Pieruschka P, Marčelja S. 1992 Statistical mechanics of random bicontinuous phases. *J. Phys. II* **2**, 235–247. (doi:10.1051/jp2:1992127)
29. Schwarz U, Gompper G. 2002 Bicontinuous surfaces in self-assembling amphiphilic systems. In *Morphology of condensed matter: physics and geometry of spatial complex systems* (eds K Mecke and D Stoyan), vol. 600, pp. 107–151. Berlin, Heidelberg: Springer. (doi:10.1007/3-540-45782-8_5)
30. Brakke KA. 1992 The surface evolver. *Exp. Math.* **1**, 141–165. (doi:10.1080/10586458.1992.10504253)
31. Barkema GT, Mousseau N. 2000 High-quality continuous random networks. *Phys. Rev. B* **62**, 4985–4990. (doi:10.1103/PhysRevB.62.4985)
32. Schröder-Turk GE, Mickel W, Kapfer SC, Schaller FM, Breidenbach B, Hug D, Mecke K. 2013 Minkowski tensors of anisotropic spatial structure. *New J. Phys.* **15**, 083028. (doi:10.1088/1367-2630/15/8/083028)
33. Mickel W, Schröder-Turk GE, Mecke K. 2012 Tensorial Minkowski functionals of triply periodic minimal surfaces. *Interface Focus* **2**, 623–633. (doi:10.1098/rsfs.2012.0007)
34. Fogden A, Hyde ST. 1999 Continuous transformations of cubic minimal surfaces. *Eur. Phys. J. B* **7**, 91–104. (doi:10.1007/s100510050592)
35. Schröder-Turk GE, Varslot T, de Campo L, Kapfer SC, Mickel W. 2011 A bicontinuous mesophase geometry with hexagonal symmetry. *Langmuir* **27**, 10 475–10 483. (doi:10.1021/la201718a)
36. OKeeffe M, Peskov MA, Ramsden SJ, Yaghi OM. 2008 The reticular chemistry structure resource (RCSR) database of, and symbols for, crystal nets. *Acc. Chem. Res.* **41**, 1782–1789. (doi:10.1021/ar800124u)
37. Blatov VA, Delgado-Friedrichs O, O'Keeffe M, Proserpio DM. 2007 Three-periodic nets and tilings: natural tilings for nets. *Acta Crystallogr. A* **63**, 418–425. (doi:10.1107/S0108767307038287)
38. Sellers SR, Man W, Sahba S, Florescu M. 2017 Local self-uniformity in photonic networks. *Nat. Commun.* **8**, 14439. (doi:10.1038/ncomms14439)
39. Schröder-Turk GE *et al.* 2013 Polycontinuous geometries for inverse lipid phases with more than two aqueous network domains. *Faraday Discuss.* **161**, 215–247. (doi:10.1039/C2FD20112G)
40. Dimitriyev MS, Reddy A, Grason GM. 2023 Medial packing, frustration, and competing network phases in strongly segregated block copolymers. *Macromolecules* **56**, 7184–7202. (doi:10.1021/acs.macromol.3c01098)
41. Grason GM, Thomas EL. 2023 How does your gyroid grow? A mesoatomic perspective on supramolecular, soft matter network crystals. *Phys. Rev. Mater.* **7**, 045603. (doi:10.1103/PhysRevMaterials.7.045603)
42. Sadoc J, Charvolin J. 1989 Infinite periodic minimal surfaces and their crystallography in the hyperbolic plane. *Acta Crystallogr. A* **45**, 10–20. (doi:10.1107/S0108767388008438)
43. Robins V, Ramsden SJ, Hyde ST. 2004 2D hyperbolic groups induce three-periodic Euclidean reticulations. *Eur. Phys. J. B* **39**, 365–375. (doi:10.1140/epjb/e2004-00202-2)
44. Pedersen MC, Hyde ST, Ramsden S, Kirkensgaard JJK. 2023 Mapping hyperbolic order in curved materials. *Soft Matter* **19**, 1586–1595. (doi:10.1039/D2SM01403C)
45. Klatt MA *et al.* 2019 Universal hidden order in amorphous cellular geometries. *Nat. Commun.* **10**, 811. (doi:10.1038/s41467-019-08360-5)
46. Pedersen MC, Hyde ST. 2018 Polyhedra and packings from hyperbolic honeycombs. *Proc. Natl Acad. Sci. USA* **115**, 6905–6910. (doi:10.1073/pnas.1720307115)

47. Goldstein R, Pesci A, Raufaste C, Shemilt J. 2021 Geometry of catenoidal soap film collapse induced by boundary deformation. *Phys. Rev. E* **104**, 035105. (doi:10.1103/PhysRevE.104.035105)
48. Hatcher A, Thurston W. 1980 A presentation for the mapping class group of a closed orientable surface. *Topology* **19**, 221–237. (doi:10.1016/0040-9383(80)90009-9)
49. Chen H. 2019 Minimal twin surfaces. *Exp. Math.* **28**, 404–419. (doi:10.1080/10586458.2017.1413455)
50. Schaller FM *et al.* 2013 Set Voronoi diagrams of 3D assemblies of aspherical particles. *Philos. Mag.* **93**, 3993–4017. (doi:10.1080/14786435.2013.834389)
51. Weis S, Schönhöfer PW, Schaller F, Schröter M, Schröder-Turk GE. 2017 Pomelo, a tool for computing generic set Voronoi diagrams of aspherical particles of arbitrary shape. *EPJ Web Conf.* **140**, 06007. (doi:10.1051/epjconf/201714006007)
52. Himmelmann M, Pedersen MC. 2025 Supplementary Code for the Manuscript “Amorphous bicontinuous minimal surface models and the superior Gaussian curvature uniformity of Diamond, Primitive and Gyroid surfaces”. Zenodo. (doi:10.5281/zenodo.17471622)
53. Himmelmann M, Pedersen MC, Klatt MA, Schönhöfer PWA, Evans ME, Schröder-Turk GE. 2025 Amorphous bicontinuous minimal surface models and the superior Gaussian curvature uniformity of Diamond, Primitive and Gyroid surfaces. Figshare. (doi:10.6084/m9.figshare.c.8174484)